ORIGINAL PAPER

# High-Temperature Oxidation of Fe$_3$Al and Fe$_3$Al–Zr Intermetallics

**S. Chevalier · P. Juzon · G. Borchardt · A. Galerie · K. Przybylski · J. P. Larpin**

**Abstract** The oxidation behavior of Fe$_3$Al and Fe$_3$Al–Zr intermetallic compounds was tested in synthetic air in the temperature range 900–1200 °C. The addition of Zr showed a significant effect on the high-temperature oxidation behavior. The total weight gain after 100 h oxidation of Fe$_3$Al at 1200 °C was around three times more than that for Fe$_3$Al–Zr materials. Zr-containing intermetallics exhibited abnormal kinetics between 900 and 1100 °C, due to the presence and transformation of transient alumina into stable α-Al$_2$O$_3$. Zr-doped Fe$_3$Al oxidation behavior under cyclic tests at 1100 °C was improved by delaying the breakaway oxidation to 80 cycles, in comparison to 5 cycles on the undoped Fe$_3$Al alloys. The oxidation improvements could be related to the segregation of Zr at alumina grain boundaries and to the presence of Zr oxide second-phase particles at the metal–oxide interface and in the external part of the alumina scale. The change of oxidation mechanisms, observed using oxygen–isotope experiments followed by secondary-ion mass spectrometry, was ascribed to Zr segregation at alumina grain boundaries.

S. Chevalier (✉) · P. Juzon · J. P. Larpin
Institut Carnot Bourgogne, UMR 5209 CNRS, Université de Bourgogne,
9 Avenue Alain Savary, BP 47870, 21078 Dijon Cedex, France
e-mail: sebastien.chevalier@u-bourgogne.fr

P. Juzon · K. Przybylski
Faculty of Materials Science and Ceramics, AGH University of Science and Technology,
al. Mickiewicza, 30-059 Cracow, Poland

G. Borchardt
Institut für Metallurgie, Technische Universität Clausthal, Robert-Koch-Strasse 42,
38678 Clausthal-Zellerfeld, Germany

A. Galerie
SIMaP, Grenoble INP, BP 75, 38402 Saint-Martin d'Hères Cedex, France

## Introduction

Iron aluminides based on $Fe_3Al$ and FeAl have emerged as good-to-exceptional corrosion–resistant alloys for elevated-temperature use in several aggressive environments [1–3], despite limited mechanical properties at room temperature [4]. Upon exposure to oxygen-containing gases, the aluminum in iron aluminides is preferentially oxidized to form a surface layer of almost pure alumina. The studies dealing with the oxidation of Fe–Al alloys [5–9] proposed that an important factor in alumina-scale formation is that the temperature must be high enough to support the formation of $\alpha$-$Al_2O_3$ rather than that of less-protective transient alumina. The quantity of aluminum remains another crucial factor [10–12] to ensure the development of a continuous alumina layer. For any oxidation-resistant alloy, the basic definition of the exposure time to breakaway failure at a given oxidation temperature is the time required for the concentration at the alloy-oxide interface of the element required to form the protective oxide scale (e.g. Al) to fall to some critical level at which protection breaks down [12, 13]. In the case of iron aluminides, if the rate of Al removal by oxidation is faster than the rate of diffusion of the element from the bulk of the alloy, it results in the breakdown of the alumina scale, owing to the formation of Fe-rich oxides.

The addition of chromium to FeAl intermetallics supports the formation and the maintenance of a continuous layer of $\alpha$-$Al_2O_3$, particularly by preventing the internal oxidation of aluminum [14, 15]. The presence of chromium in ternary alloys can decrease the percentage of aluminum necessary to the development of a continuous and protective layer and leads to accelerated formation of alumina [16, 17]. A reduction of the aluminum level improves ductility; so, Cr additions have positive effects on both mechanical properties and high-temperature corrosion resistance of a variety of intermetallics [18]. Moreover, the presence of Cr accelerates the transformation from $\theta$- to $\alpha$-$Al_2O_3$, which considerably reduces the oxidation rates and retards fast outward Al diffusion for $\theta$-$Al_2O_3$ scale growth. Therefore, Cr addition is believed to play a role in eliminating interfacial voids and improving oxide–scale adherence [19, 20].

Intermetallics protective behavior with respect to oxidation at high temperatures is directly connected to the oxide scale adherence, especially when industrial applications involve thermal cycles. The most effective way to improve oxide–layer adherence is adding small quantities of reactive elements (RE) such as Hf, Y, Zr, etc., able to form thermodynamically stable oxides [21–24]. Indeed, the addition of such elements improves the adherence of the oxide scale, and even slows down their growth rate. Thus, RE additions as alloying elements in the alloys are of major importance to improve their oxidation resistance, leading to beneficial effect, called "Reactive-Element Effect" (REE). In a general way, the main REE for alumina-forming alloys is a huge improvement of the oxide–scale adherence to the metallic

substrate [25–35]. This beneficial effect is also observed for iron aluminides, such as FeAl [6, 8, 9] and Fe$_3$Al [36–39] intermetallics.

At temperatures close to 1100 °C, $\alpha$-Al$_2$O$_3$ can grow by mixed diffusion of anions and cations. Previous studies suggested that the presence of RE could modify the diffusion mechanism and then the oxidation mechanism [27] by segregating at alumina grain boundaries [40]. Results of two-stage oxidation experiments under $^{16}$O$_2$ and $^{18}$O$_2$ showed that external diffusion of cations could be blocked by RE additions [23, 28–30, 33, 41–46]. Even if oxygen diffusion is still available in RE-doped $\alpha$-Al$_2$O$_3$, oxygen diffusion coefficients at oxide grain boundaries decrease [47, 48], especially in the presence of Y$_2$O$_3$.

The aim of the present study was to oxidize Fe$_3$Al and Fe$_3$Al–Zr intermetallic compounds under isothermal conditions in synthetic air in the temperature range 900–1200 °C and under cyclic conditions at 1100 °C. The corrosion products were characterized by scanning-electron microscopy (SEM) coupled with energy-dispersive X-ray analyses (EDX), X-ray diffraction (XDR), photoluminescence (PLS) and transmission-electron microscopy (TEM). The growth mechanisms were analyzed with the help of two-stage oxidation experiments in $^{16}$O$_2$ followed by $^{18}$O$_2$, completed by secondary-ion mass spectrometry (SIMS) to get oxygen–isotope distribution profiles in the alumina scales.

## Experimental Procedures

The base materials used for the experiments were iron aluminides with the addition of supplementary elements (Cr, Zr, B, and C) provided by Military University of Technology in Warsaw (Poland). The chemical compositions of the Fe$_3$Al-modified elements are listed in Table 1.

The alloys were melted in a Balzers induction furnace in an argon atmosphere and cast into graphite molds (with a diameter of 25 mm and a length of 500 mm). The samples were homogenized at 1100 °C for 5 h, followed by hot forging at 1100 °C and hot rolling at 650–750 °C (obtained tape with 12 mm width and thickness about 1 mm). The specimen microstructure consisted of grains having an average size 200–250 μm.

Specimens cut from the ingots were approximately 10 × 10 × 1 mm in size. They were manually ground using SiC abrasive paper down to 1200 grade, then, ultrasonically cleaned in ethanol, dried at room temperatures, and weighed.

Oxidation experiments were performed using a continuous thermogravimetric method (Setaram TGA 92), where weight gains were measured as a function of

**Table 1** Chemical composition of Fe$_3$Al alloys (at.%) (Fe balance)

| Alloy | Element (at.%) | | | | | | | |
|---|---|---|---|---|---|---|---|---|
| | Al | Cr | Zr | Mo | B | Nb | C | Fe |
| Fe$_3$Al | 28.0 | 5.0 | – | – | 0.005 | – | 0.03 | Bal. |
| Fe$_3$Al–Zr | 28.0 | 5.0 | 0.05 | – | 0.005 | – | 0.03 | Bal. |

time. The reactive environment was synthetic air (AIR LIQUIDE gas) with a flow rate of ~50 mL/min, under atmospheric pressure over the temperature 900–1200 °C for 100 h.

Cyclic oxidation was used to estimate the adherence of the oxide scale. Cyclic-oxidation experiments were performed in a muffle furnace (LENTON) at 1100 °C in laboratory air under atmospheric pressure. One cycle consisted of 24 h heating followed by rapid cooling to room temperature for approximately 20 min. Gross and net weight changes were recorded. The net weight gain corresponds to the specimen weight excluding the spalled particles weight. The gross weight gain corresponds to the specimens weight together with their eventual spalled oxides collected in the crucible. The difference between the net and the gross weight gains indicated the proportion of spalled oxide particles [49]. The cyclic-oxidation tests were performed up to ~3000 h (120 × 24 h-cycles). The experiments were shortened if the samples behaved catastrophically.

The morphology, structure and chemistry of the oxidized specimens were investigated using JEOL JSM-6400F scanning-electron microscopy (SEM) equipped with a field-emission gun (FEG) and coupled with an energy-dispersive X-Ray analyzer (EDX). A second SEM Philips XL30, coupled with an EDX analyzer was used for determination the element distribution across the oxide layer.

Transmission-Electron Microscopy (TEM) observations were carried out using a 200 kV field-emission gun microscopes (Tecnai F20 S-Twin) and a $LaB_6$ microscope (JEOL 2100), equipped with energy-dispersive X-ray (EDX) for chemical analyses. TEM specimens were prepared by focused-ion-beam (FIB) milling (Quanta 200 3D DualBeam FIB/SEM).

Two-stage oxidation experiments (in $^{16}O_2/^{18}O_2$), followed by secondary-ion mass spectrometry (SIMS), was used to elucidate the alumina-scale growth mechanism [49]. Sequential oxidation experiments were processed by oxidizing firstly Fe₃Al specimens under 200 mbar $^{16}O_2$ pressure. The oxidant atmosphere was then evacuated and replaced by $^{18}O_2$ (isotopic purity of about 90%) under the same pressure. The samples were not cooled between the two steps of the oxidation test to avoid any thermal shocks, which could cause cracks and/or spallation of the oxide scales. After the second oxidation stage, the oxidizing atmosphere was evacuated to reach a low pressure and the samples were quickly removed outside the furnace to be cooled to room temperature. Experimental conditions (Table 2) were chosen in order to obtain an oxide scale without cracks and with the same thickness after oxidation in $^{16}O_2$ and the same thickness after oxidation in $^{18}O_2$ [29, 50, 51].

Secondary-ion mass spectrometry (SIMS) profiles were made with a MIQ 256 Riber analyzer using 10 keV, 50 nA intensity, $Ar^+$ beam as the primary ion beam.

| Alloy | T [°C] | Duration under $^{16}O_2$ [h] | Duration under $^{18}O_2$ [h] |
|-------|--------|-------------------------------|-------------------------------|
| Fe₃Al | 900 | 4 | 48 |
| Fe₃Al | 1100 | 2 | 6 |
| Fe₃Al–Zr | 900 | 4 | 48 |
| Fe₃Al–Zr | 1100 | 2 | 6 |

Table 2 Experimental conditions for the two stage oxidation experiments under $^{16}O_2/^{18}O_2$

The angle of incidence was 45°; the size of the total crater was 95 μm × 135 μm, and the analyzed zone was 10% of that crater.

The phase compositions of oxide formed on the surface of the oxidized samples were identified by X-ray diffraction (XRD) using Cu $K_\alpha$ ($\lambda$ = 0.154 nm) or Co $K_\alpha$ ($\lambda$ = 0.1789 nm) radiation. Various grazing angles were chosen in order to obtain phase information from the whole oxide layer thickness.

The phase compositions of oxide formed on the surface of the oxidized samples were identified by $Cr^{3+}$ fluorescence, analyzing the rays reflected from the scale surface. The luminescence spectroscopy was performed using an optical microprobe enabling a laser beam (Spectra-Physics RM2018 power 20 mW) to be focused onto features identified in the microscope and their luminescence spectra recorded. In the study, an argon (514.5 nm) laser excitation was used. The photoluminescence was collected by the objective lens of the microscope, passed through a Jobin-Yvon T64000 spectrometer and the spectrum detected with a CCD detector. The recorded spectrum was fitted and analyzed using the commercial GRAM software.

## Results

Isothermal Oxidation of Fe$_3$Al

### Oxidation Kinetics

The oxidation-kinetics curves of Fe$_3$Al alloy are plotted in Fig. 1a, showing the mass gains versus time at temperatures between 900 °C and 1200 °C. The weight gains increase typically with temperature. The common way to compare measured oxidation behavior with that of other materials and/or the behavior at other temperatures are to determine the parabolic rate constant $k_p$, based on the assumption that the oxidation rate obeys the classical parabolic rate law. Values of $k_p$ were calculated from plots of mass-change data versus square root of time. Activation energy for were determined from the plot of parabolic rate law constants ($k_p$) in an Arrhenius diagram.

For Fe$_3$Al at 1000 °C and below, the plots of the mass-change data exhibited two distinct oxidation stages with a rapid oxidation in the initial stage followed by a slower oxidation. The parabolic rate constants here are termed by $k_p^{1st}$ (for the initial oxidation stage between 1 and 10 h) and $k_p^{2nd}$ (for the later stage), respectively. At higher temperature, the initial oxidation stage was shorter. At temperatures above 1100 °C the parabolic rate constants tended to decrease with oxidation time, what is associated with the coarsening of the oxide grains. The oxidation obeyed a parabolic rate law throughout the temperatures, except a somewhat rapid mass gain in the very initial stages (up to 1 h). For comparison, Table 3 summarizes the parabolic rate constants $k_p$ at each temperature for Fe$_3$Al, with $k_p^{1st}$ for the initial oxidation stage and $k_p^{2nd}$ for the later stage.

Figure 2a shows Arrhenius plots (log $k_p$ vs. 1/T) of the parabolic rate constants ($k_p^{1st}$ and $k_p^{2nd}$) for the Fe$_3$Al. At temperatures around 950 °C both $k_p^{1st}$ and $k_p^{2nd}$ are given in this plot. Activation energies for the $k_p^{1st}$ and $k_p^{2nd}$ are 82 and 712 or 154 (correspond to 900–1100 °C or 1100–1200 °C) kJ mol$^{-1}$, respectively. The values
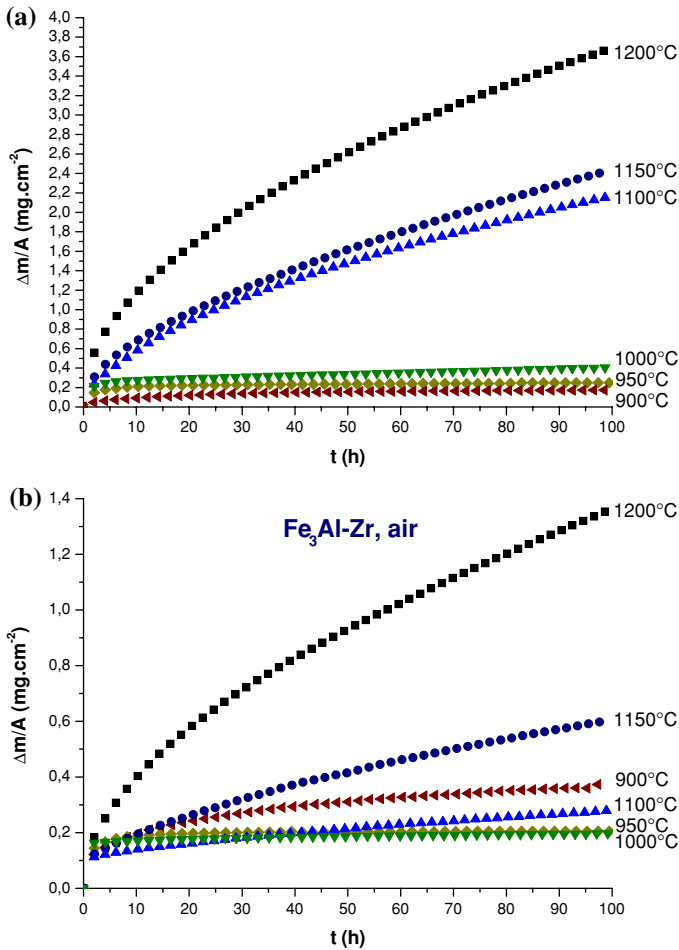
**Fig. 1** Isothermal oxidation kinetics curves in the temperature range 900–1200 °C in air under atmospheric pressure, **a** for Fe$_3$Al and **b** for Fe$_3$Al–Zr

appear somewhat different than the values generally obtained for alumina-formation kinetics (around 250 kJ mol$^{-1}$ [36]). But, most of studies did not separate Arrhenius plots in several domains. Babu et al. found an activation energy of 92 kJ mol$^{-1}$ for oxidation kinetics of Fe25Al [52]. The k$_p$ values collected from the present kinetics data are in agreement with those of the literature [53].

*Oxide-Scale Characterization*

Figure 3 shows the surface morphologies of Fe$_3$Al oxidized for 100 h in the temperature range 900–1200 °C. On all samples, EDX analyses identified Al and O.

At 900 °C, the oxide surface is composed of well developed plate-like crystals typical of transient alumina. The same morphology is observed at 950 °C, despite

**Table 3** Parabolic rate constants for the Fe₃Al and Fe₃Al–Zr oxidized at temperatures between 900 °C and 1200 °C in air under an isothermal condition

| | $k_p^{1st}$ (g$^2$ cm$^{-4}$ s$^{-1}$) | $k_p^{2nd}$ (g$^2$ cm$^{-4}$ s$^{-1}$) | $\Delta m/A$ after oxidation for 100 h (mg cm$^{-2}$) |
|---|---|---|---|
| **Fe₃Al** | | | |
| 900 °C | $7.5 \times 10^{-13}$ | – | 0.17 |
| 950 °C | $1.1 \times 10^{-12}$ | $6.8 \times 10^{-15}$ | 0.25 |
| 1000 °C | $1.5 \times 10^{-12}$ | $1.4 \times 10^{-13}$ | 0.40 |
| 1100 °C | | $1.5 \times 10^{-11}$ | 2.15 |
| 1150 °C | | $2.1 \times 10^{-11}$ | 2.40 |
| 1200 °C | | $3.8 \times 10^{-11}$ | 3.66 |
| **Fe₃Al–Zr** | | | |
| 900 °C | $5.4 \times 10^{-14}$ | – | 0.37 |
| 950 °C | $1.4 \times 10^{-13}$ | $4.6 \times 10^{-16}$ | 0.20 |
| 1000 °C | $4.4 \times 10^{-13}$ | $3.3 \times 10^{-15}$ | 0.20 |
| 1100 °C | | $1.6 \times 10^{-13}$ | 0.28 |
| 1150 °C | | $1.3 \times 10^{-12}$ | 0.60 |
| 1200 °C | | $6.1 \times 10^{-12}$ | 1.35 |

scale spallation exposing metallic substrate. Oxide grains become apparent below the platelets (Fig. 3b). Oxidation at 1000 °C produced wrinkling and cracking of the scale, which partially spalled off during cooling to room temperature. Wrinkling was already observed by Yhang et al. [54] who attributed it to different diffusivity in the alloy. The surface is composed mainly of small geometric grains (Fig. 3c), generally described in the literature as alpha alumina [55]. At higher temperature (1100, 1150 and 1200 °C) the scale exhibits convoluted, network-like structure (Fig. 3d–f). Ridge morphology with pores exhibits small amount of needle- or whisker-like oxides extruding out of the surface scale, especially at 1150 °C (Fig. 3e). Cross-sections showed that the wrinkled oxide scale consisted of coarse equiaxed grains.

XRD analyses of all investigated samples after oxidation reveal that the oxide formed at 900 °C and 950 °C consist of $\alpha$-Al$_2$O$_3$ with some of $\theta$-Al$_2$O$_3$, while at 1000 °C and higher temperatures only $\alpha$-Al$_2$O$_3$ was found (Table 4). These results suggest that for Fe₃Al the phase transformation of $\theta$-Al$_2$O$_3$ to $\alpha$-Al$_2$O$_3$ occurs at temperatures around 950 °C.

For samples oxidized at 900 °C and 1100 °C, the investigations of the phase composition was repeated using the method of $Cr^{3+}$ fluorescence, analyzing the rays reflected from the scale surface. Alpha and theta alumina were detected on sample oxidized at 900 °C, while only $\alpha$-Al$_2$O$_3$ was detected on sample from 1100 °C (Fig. 4).

Isothermal Oxidation of Fe₃Al–Zr

*Oxidation Kinetics*

Figure 1b shows the mass gain per unit surface area changes for Fe₃Al–Zr oxidized in synthetic air at temperatures between 900 and 1200 °C. Parabolic kinetics are
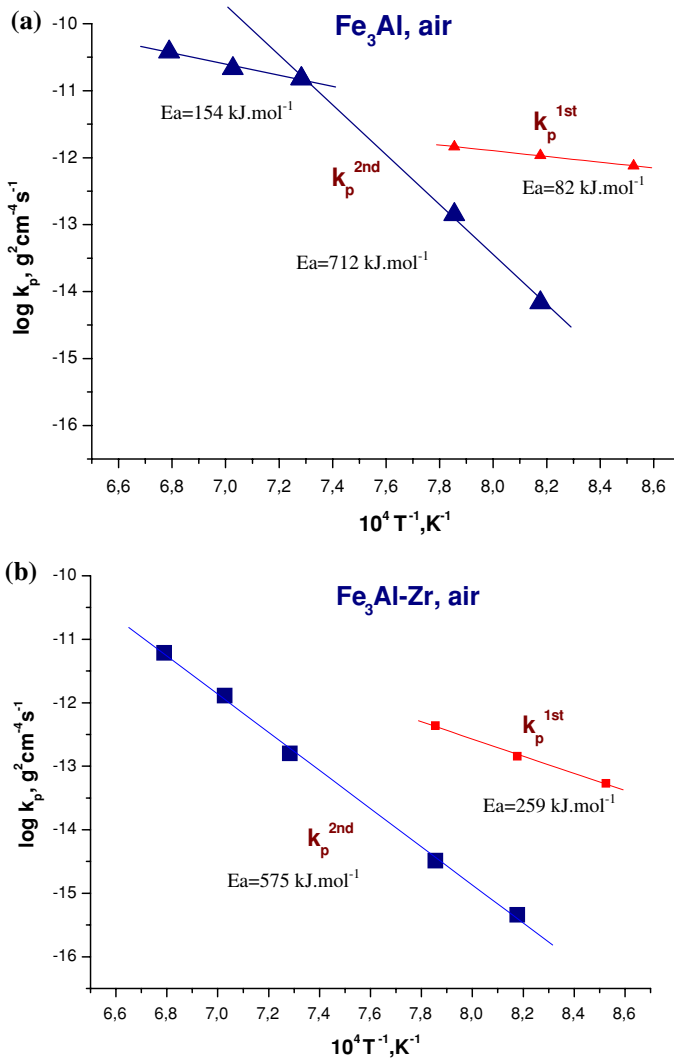
**Fig. 2** Arrhenius plots of the parabolic rate constant $k_p^{1st}$ and $k_p^{2nd}$, **a** for $Fe_3Al$ and **b** for $Fe_3Al$–Zr

observed and the oxidation process seems to be thermally activated. However, plots indicate abnormal order. Exposure at 900 °C produces weight gains higher than that produced at 950 °C, 1000 °C and 1100 °C after a critical few hours (10 h). This phenomenon has been reported previously [56]. At temperatures 1000 °C and below, the parabolic rate constants were calculated for the initial oxidation stage between 2 and 10 h ($k_p^{1st}$) and for the later stage ($k_p^{2nd}$). At higher temperature, the initial oxidation stage was shorter, only $k_p^{2nd}$ was measured. The oxidation obeyed a parabolic rate law, except the stages up to 1 h. Table 3 summarizes the parabolic rate constants ($k_p$) obtained at each temperature for $Fe_3Al$–Zr, with $k_p^{1st}$ for the initial
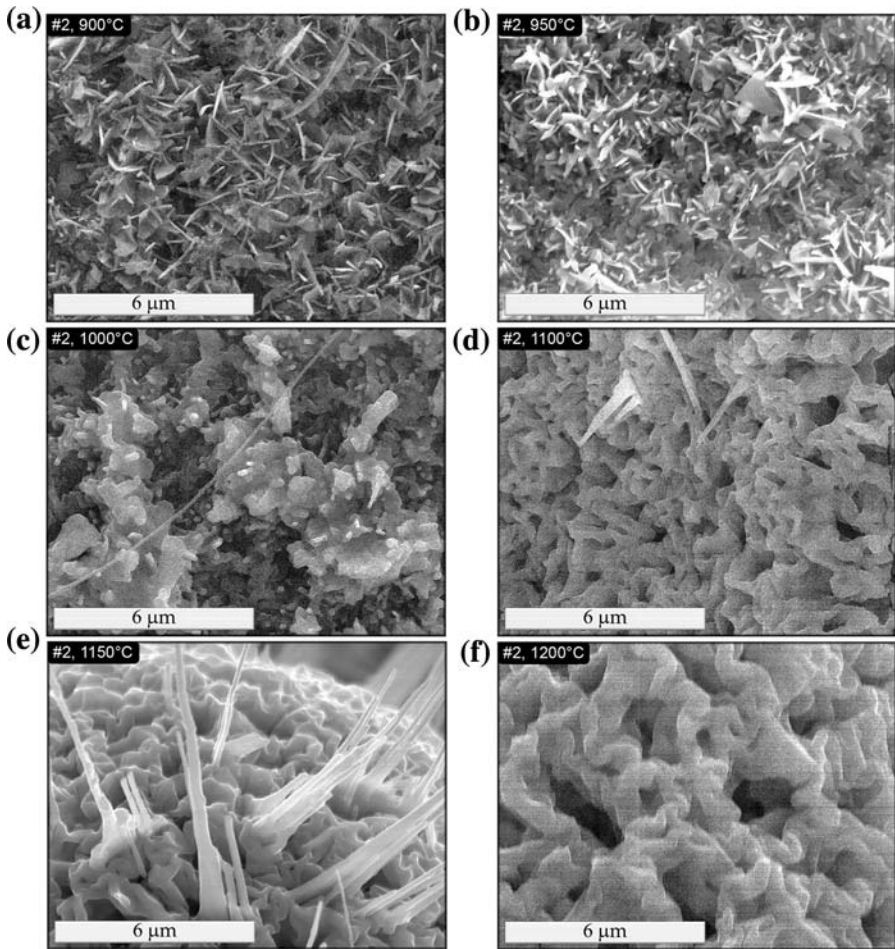
**Fig. 3** SEM micrographs of the scale formed on Fe₃Al in air after 100 h at range 900–1200 °C

oxidation stage and $k_p^{2nd}$ for the later stage. Activation energies for the $k_p^{1st}$ and $k_p^{2nd}$ obtained from Arrhenius plots (Fig. 2b) are 259 and 575 kJ mol$^{-1}$, respectively.

*Oxide Scale Characterization*

The evolution of the oxide-scale morphology of the Fe₃Al–Zr after oxidation for 100 h at temperatures between 900–1200 °C is shown in Fig. 5.

At 900 °C, the scale is composed of blade-like crystals (Fig. 5a). No spallation is observed at 950 °C. The scale consists of a mixture of transient and $\alpha$-Al₂O₃ grains (Fig. 5b). Oxidization at 1000 °C produced slight spallation. The oxide layer consisted of different-length grains, but looks similar to the scale grown at 950 °C (Fig. 5c). At 1100 and 1150 °C (Fig. 5d, e), a ridge-type structure is observed with

**Table 4** XRD of oxide phase grown on Fe$_3$Al and Fe$_3$Al–Zr intermetallics

|  | Oxide phases |
|---|---|
| Fe$_3$Al | |
| 900 °C | $\theta$-Al$_2$O$_3$, $\alpha$-Al$_2$O$_3$ |
| 950 °C | $\theta$-Al$_2$O$_3$, $\alpha$-Al$_2$O$_3$ |
| 1000 °C | $\alpha$-Al$_2$O$_3$ |
| 1100 °C | $\alpha$-Al$_2$O$_3$ |
| 1150 °C | $\alpha$-Al$_2$O$_3$ |
| 1200 °C | $\alpha$-Al$_2$O$_3$ |
| Fe$_3$Al–Zr | |
| 900 °C | $\theta$-Al$_2$O$_3$, $\alpha$-Al$_2$O$_3$ |
| 950 °C | $\alpha$-Al$_2$O$_3$ |
| 1000 °C | $\alpha$-Al$_2$O$_3$ |
| 1100 °C | $\alpha$-Al$_2$O$_3$ |
| 1150 °C | $\alpha$-Al$_2$O$_3$ |
| 1200 °C | $\alpha$-Al$_2$O$_3$ |

some pores. The oxide scale exhibits a network-like structure with pores, and no bladelike grains are observed. Moreover, intensive spalling of the oxide scale from the metallic substrate is observed. Oxidation at 1200 °C produces a similar microstructure, except that the oxide grains appear to be larger and more developed. A fracture section of this sample revealed a duplex structure of the oxide scale. Good, adherent-to-metallic-substrate columnar grains are covered by fine equiaxed grains (Fig. 5f).

At all temperatures the scale consists of $\alpha$-Al$_2$O$_3$, while $\theta$-Al$_2$O$_3$ appears only at 900 °C (see Table 4). The relative peak intensities of $\alpha$-Al$_2$O$_3$ are increasing with oxidation temperature.

Figure 6 shows fluorescence spectra of Al$_2$O$_3$ scales grown on Fe$_3$Al–Zr alloy at 900 °C in air for 1, 6, 24 and 100 h. Alpha and theta alumina are detected by respective doublets. Intensities of fluorescence spectra increase with oxidation time.

TEM investigations were used to determine the reactive-elements location within the thermally grown alumina scale. Figure 7a–c are TEM bright-field (BF) images showing the microstructure of the alumina scales formed on Fe$_3$Al–Zr alloy after 100 h oxidation in air at 1100 °C. Large columnar grains (about 1 μm wide and 0.6–0.8 μm long) develop at the alloy/scale interface (Fig. 7a) and fine-grain scale in the outer part of alumina scale (Fig. 7b). The oxide grain size at the scale/gas interface remains very fine (about 200 nm). Figure 7c is a STEM image using high-angle annular dark-field (HAADF) detector (atomic number contrast-Z contrast) which shows ZrO$_2$ particles (50–150 nm in diameter) located in the alumina scale close to the scale/alloy interface (point 2, 4). Zr could not be detected inside the Al$_2$O$_3$ grains. But, Zr is found to segregate at alumina grain boundaries, as shown by the EDX analyses performed at columnar alumina grain boundaries (spot size of 1 nm) in Fig. 8.
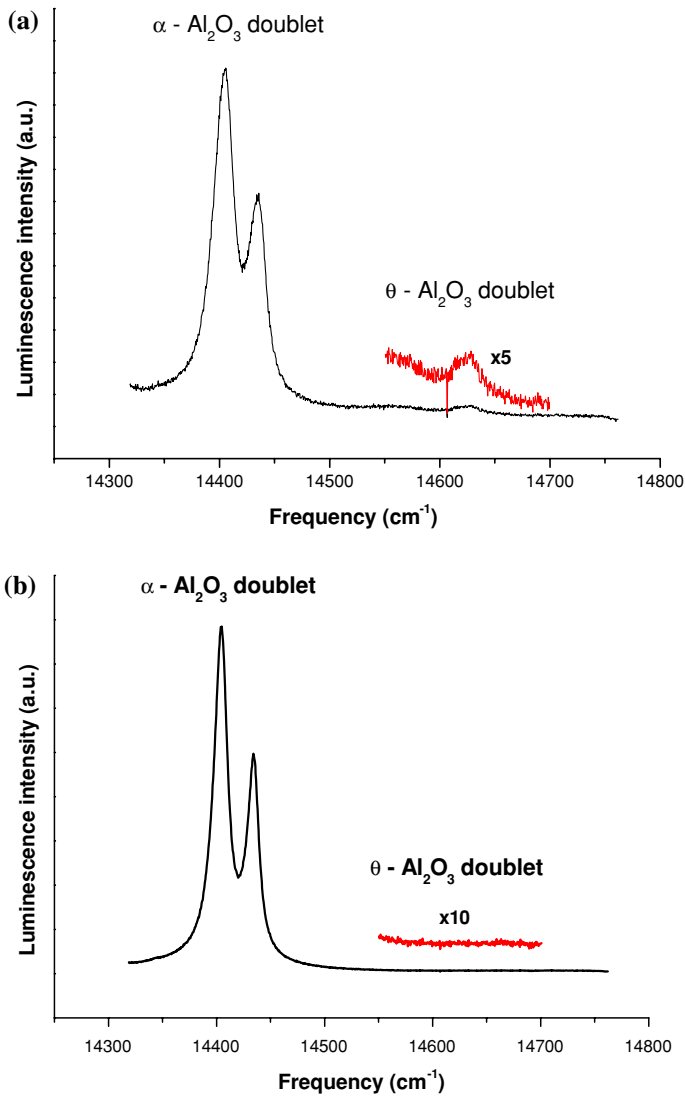
**Fig. 4** Fluorescence spectra of $Al_2O_3$ scales grown on $Fe_3Al$ in air for 100 h at: **a** 900 °C and **b** 1100 °C

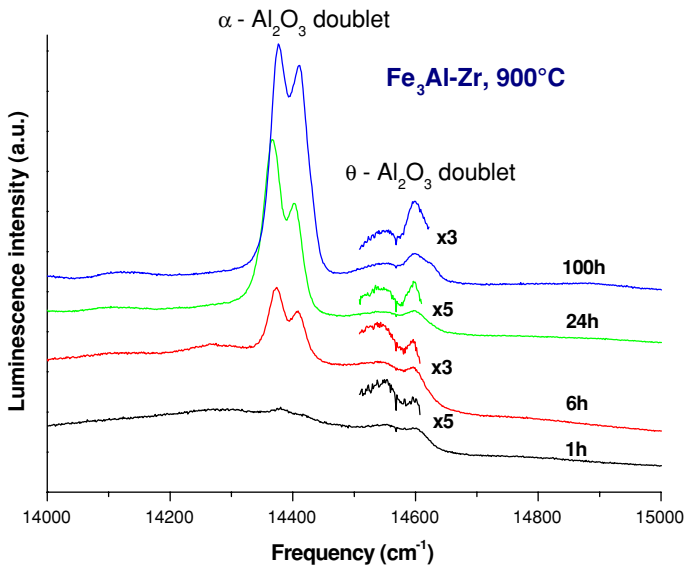## Cyclic Oxidation

### Oxidation Kinetics

The 24 h-oxidation cycles were conducted under atmospheric pressure in laboratory air at 1100 °C with the samples held in alumina crucibles. Collected gross and net weight changes are presented in Fig. 9. For undoped $Fe_3Al$ rapid mass gain of breakaway oxidation occurred from the first cycle. Almost vertical kinetics curve is
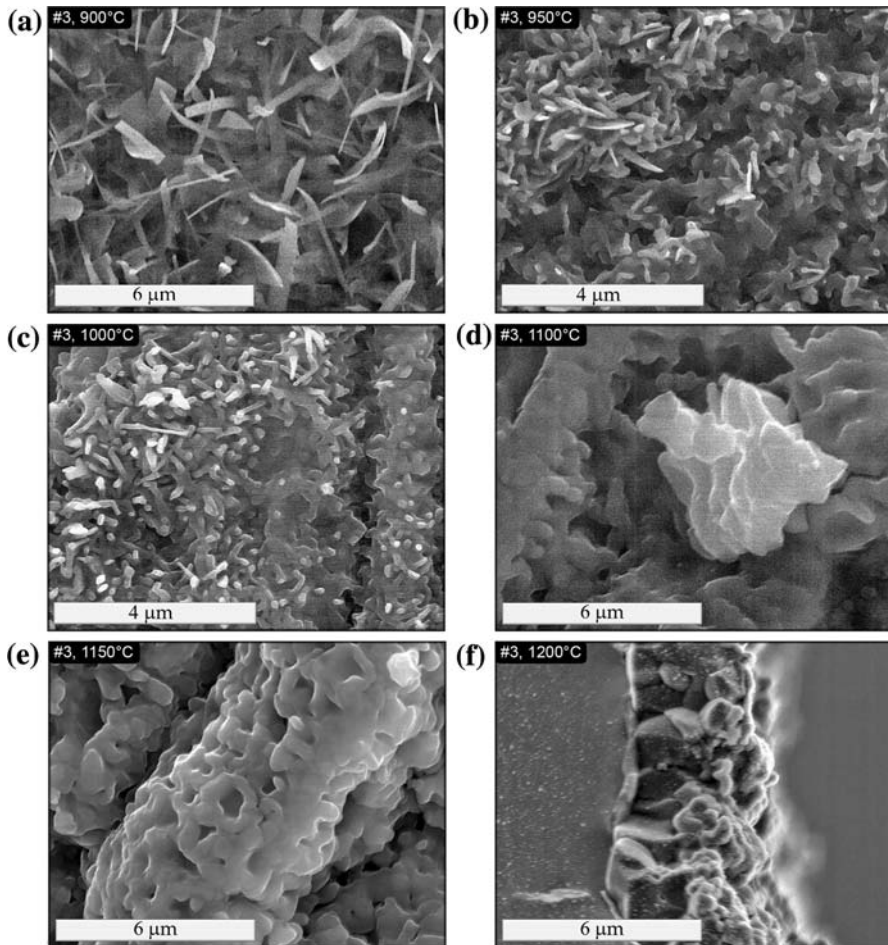
Fig. 5 SEM micrographs of the scale formed on Fe₃Al–Zr in air after 100 h between 900 and 1200 °C

observed from the beginning of the cyclic oxidation test. This exhibited a loss of the protectiveness of the thermally grown alumina scale. The net and the gross weight-gain curves close to each other during oxidation indicated sparse weight loss. Despite this bad behavior, the cyclic oxidation was carried out for 66 cycles (i.e. 1584 h).

Cyclic-oxidation kinetics for Fe₃Al–Zr alloy show that the net and the gross weight–gain curves are superimposed during the first 10 cycles. This indicates good adherence of the oxide scale. After 10 cycles, the increasing gap between the net and the gross weight–gain curves indicates that the oxide scale starts to spall. Spallation is extended after about 30 cycles (i.e. 720 h), which corresponds to that previously observed by Pint et al. [38] for 1 h-cycle at 1100 °C. A breakaway is observed after 80 cycles (i.e. 1920 h).

Fig. 6 Fluorescence spectra of $Al_2O_3$ scales grown on Fe$_3$Al–Zr at 900 °C in air for 1, 6, 24 and 100 h

## Oxide Scale Characterization

Micrographs of the surface morphology of all specimens tested from cyclic oxidation at 1100 °C are shown in Fig. 10. For undoped Fe$_3$Al massive spallation results in a significant Al loss after about 3 cycles, and formation of iron oxide scale (Fig. 10a). Further cycle tests causes destruction of the sample. Figure 10b shows the surface morphology of Fe$_3$Al after 66 cycles. The whole sample consists of iron oxide with a "hedgehog"-like morphology and cracks. The undoped sample seems to have turned into a block of iron oxide after a few cycles.

After 3 cycles, the Fe$_3$Al–Zr alloy forms flat, uniform alumina scale with good adherence to metallic substrate (Fig. 10c). Iron–oxide crystals are observed but after a longer oxidation time and not on the whole surface of the specimen, but near the corners and edges only (Fig. 10d).

The results of XRD analyses (Table 5) are in agreement with the SEM observations; Fe$_2$O$_3$ is observed after a few cycles on undoped Fe$_3$Al, but is delayed to 80 cycles on Fe$_3$Al–Zr.

## Two-Stage Oxidation Experiments

On the Fe$_3$Al specimen oxidized at 900 °C, SIMS profiles show that $^{18}O$ is located mainly close to the external interface (Fig. 11a), suggesting a mechanism with predominant outward aluminum diffusion. At 1100 °C (Fig. 11b), a major $^{18}O$ peak is located close to the external interface. There is also $^{18}O$ within $^{16}O$, which suggests mixed diffusion.
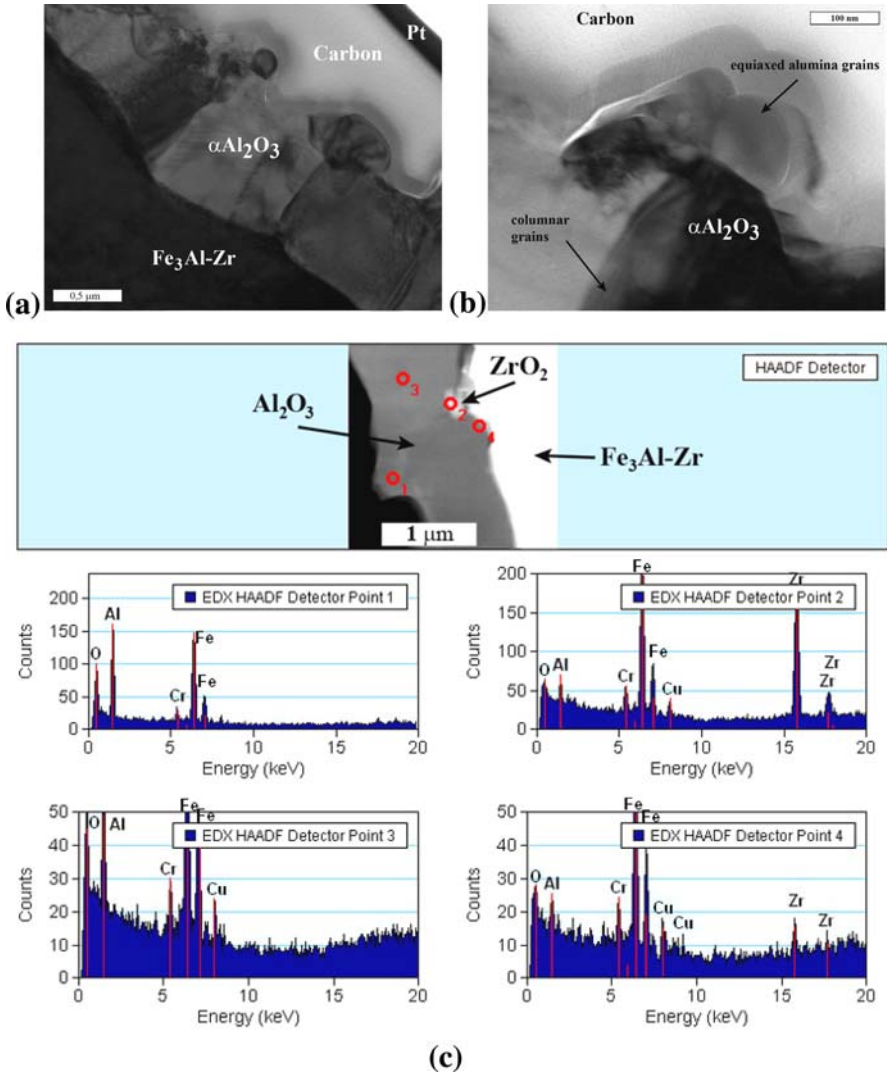
**Fig. 7** TEM cross-section images: **a** of the alumina scale formed on $Fe_3Al$–Zr after oxidation at 1100 °C in air for 100 h, **b** high magnification of the selected area showing that small equiaxed alumina particles grew on the well-developed columnar grains and **c** STEM image and EDX analyses (points 1, 2, 3, 4) in the alumina scale

On $Fe_3Al$–Zr specimen oxidized at 900 °C, SIMS results show that after the two-stage experiment most of the new oxide with $^{18}O$ formed at the external interface (Fig. 12a), suggesting that the oxide-growth mechanism involve major cationic diffusion. At 1100 °C, a large $^{18}O$ peak, found below the $^{16}O$ signal, clearly shows that the new oxide is formed at the internal interface (Fig. 12b). The alumina scale is in this case growing by predominant inward-anionic diffusion. The increase of the
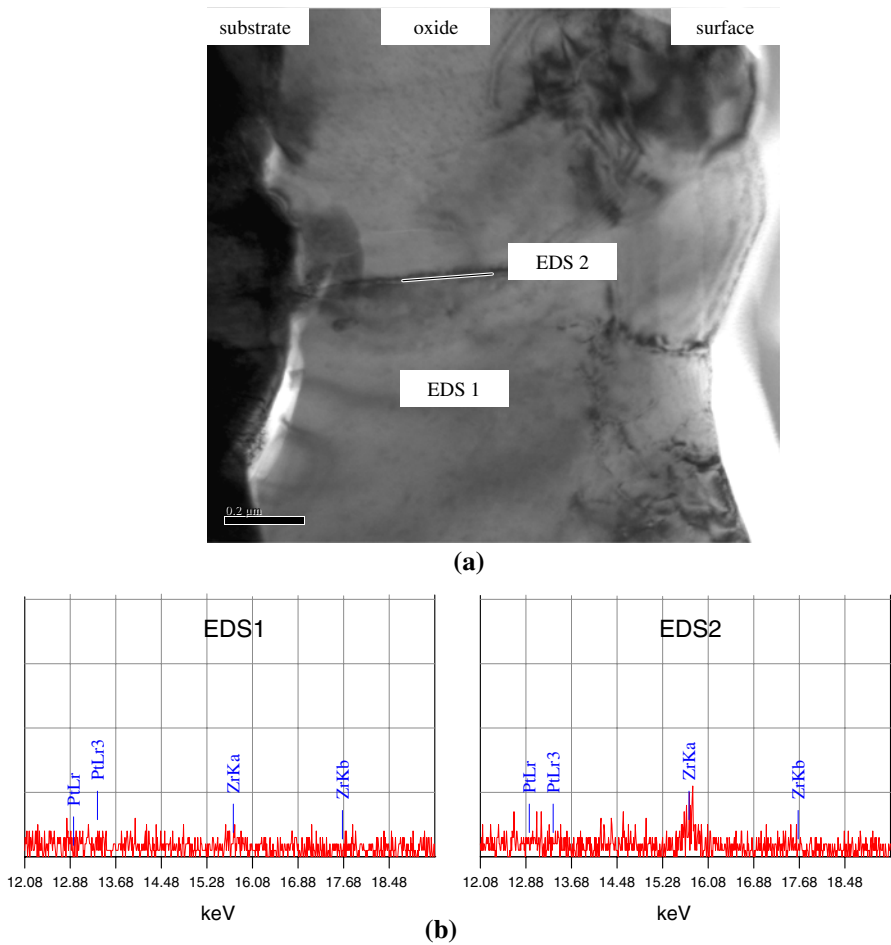
**Fig. 8** TEM cross-section and EDX analyses in alumina grains (EDS1) and at grain boundaries (EDS2) on Fe$_3$Al–Zr after oxidation at 1100 °C in air for 100 h

$^{18}$O peak close to the gas–oxide interface can be related to the presence of the equiaxed grains thin layer observed in the TEM cross-sections [51].

## Discussion

Concerning isothermal tests, for all samples, essentially parabolic kinetics were observed, and the oxidation process is thermally activated. However, the weight gains of undoped Fe$_3$Al typically increased with temperature, while this was not the case between 900 and 1000 °C for Zr-doped alloys. Fe$_3$Al–Zr exposure at 900 °C produced weight gains which became higher than those produced at 950 °C,
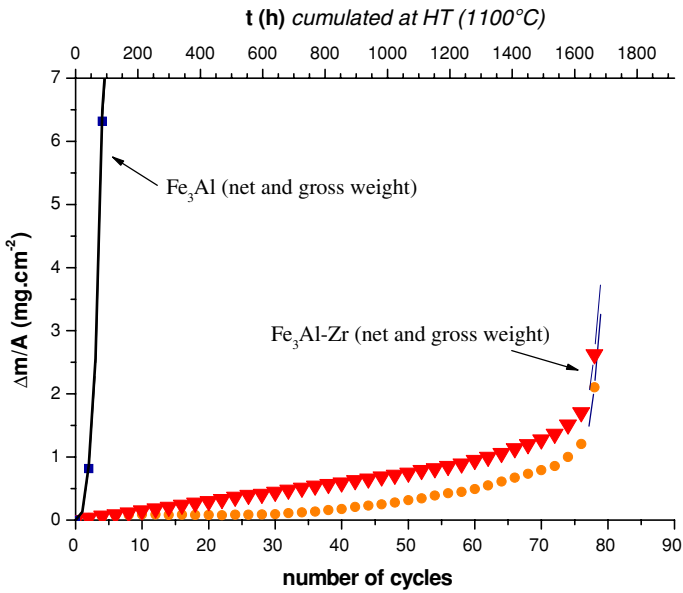
**Fig. 9** Cyclic-oxidation kinetics at 1100 °C in air, curves of mass (gross and net) change as a function of the heating time for Fe₃Al and Fe₃Al–Zr
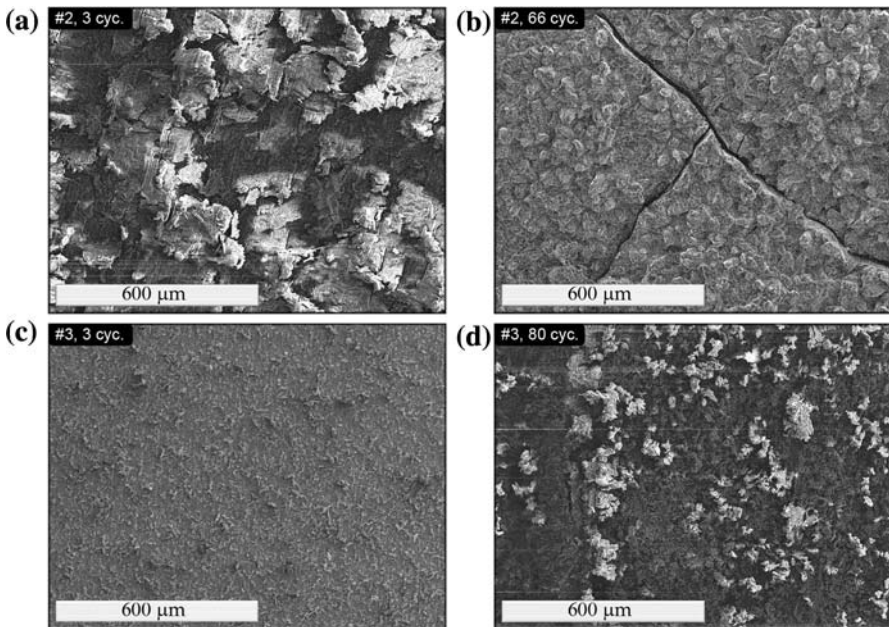


**Fig. 10** SEM pictures of Fe₃Al (**a**, **b**) and Fe₃Al–Zr (**c**, **d**) after cyclic-oxidation at 1100 °C

**Table 5** XRD of oxide phase grown during cyclic oxidation experiments at 1100 °C in air

| Alloy | Cycles | Major phases |
|---|---|---|
| $Fe_3Al$ | 3 | $Fe_2O_3$, $\alpha$-$Al_2O_3$ |
| $Fe_3Al$ | 66 | $Fe_2O_3$ |
| $Fe_3Al$–Zr | 3 | $\alpha$-$Al_2O_3$ |
| $Fe_3Al$–Zr | 80 | $Fe_2O_3$, $\alpha$-$Al_2O_3$ |
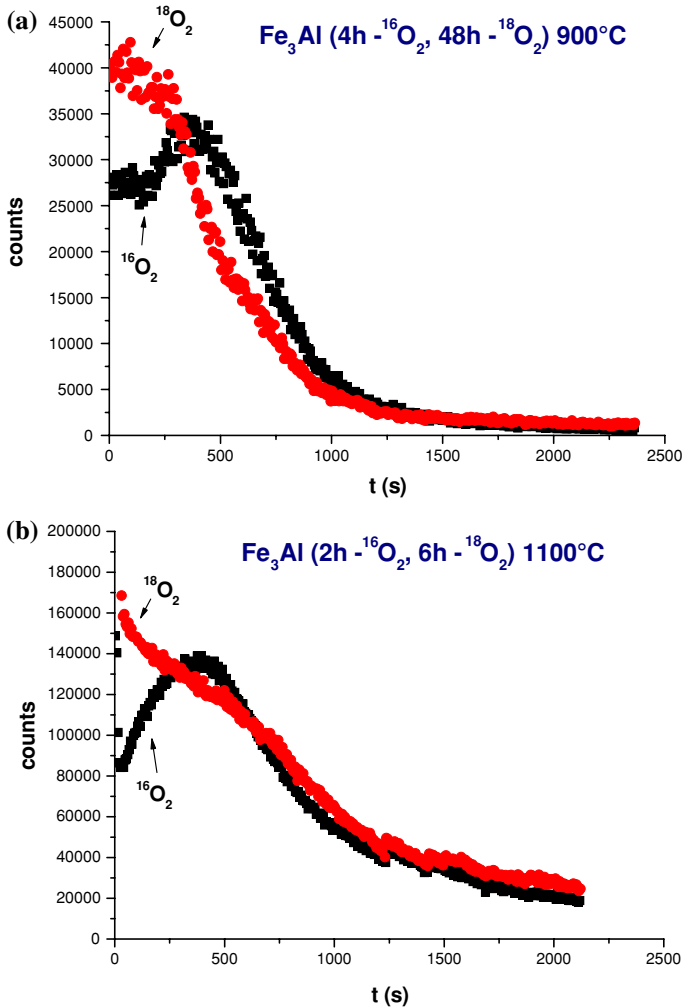


**Fig. 11** SIMS oxygen-isotope profiles for $Fe_3Al$ after two-stage oxidation experiments: **a** at 900 °C, **b** at 1100 °C

1000 °C and even 1100 °C. These observations could be connected with transient-alumina formation. Short and fast oxidation into transient alumina occurred at the beginning of the tests and the resulting mass change was larger than that associated

**(a)**



**(b)**
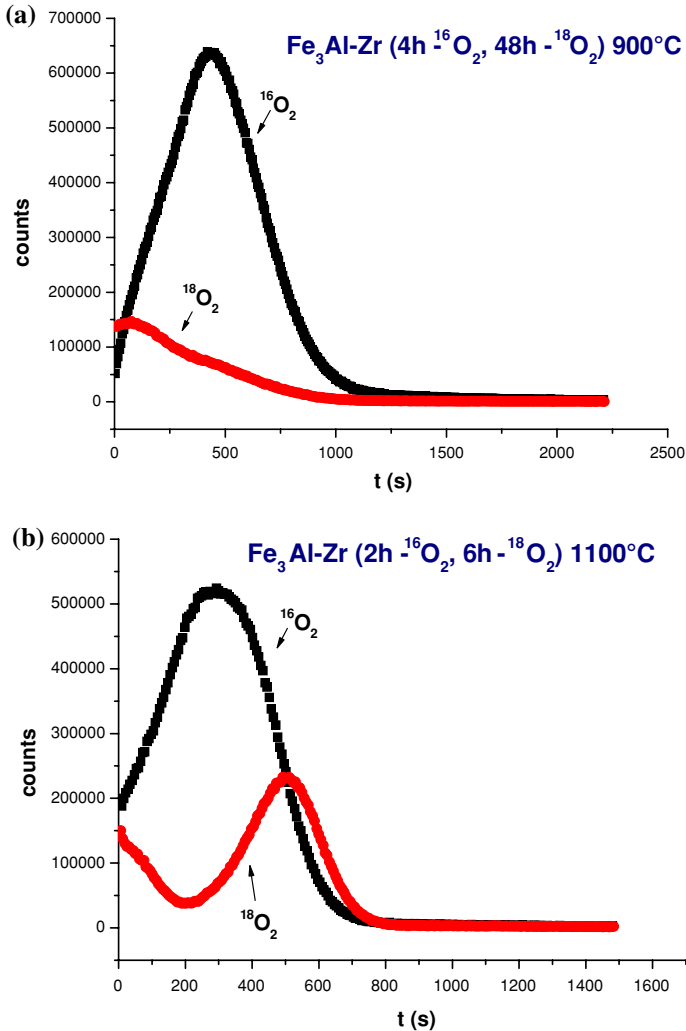
**Fig. 12** SIMS oxygen-isotope profiles for Fe$_3$Al–Zr after two-stage oxidation experiments: **a** at 900 °C, **b** at 1100 °C

with the subsequent parabolic kinetics [57]. But, the presence of RE makes it possible for α-Al$_2$O$_3$ to be quickly established instead of transient aluminas during the initial stage of the alumina-former alloys oxidation [58–60].

In order to derive values of activation energy for each growing alumina phase, most authors divided the weight–gain temperature curves into two or more stages [61–65]. Rybicki et al. [62] reported that the phase transformation from θ- to α-Al$_2$O$_3$ occurred after 8 h, when Ni–Al(Zr) alloy was oxidized at 1000 °C in air. However, this transformation strongly depended on the oxidation temperature. In this work, activation energies were calculated for the initial and later stages which

correspond to transient and α-$Al_2O_3$, respectively. Results are in good agreement with other investigators, which reported values of 400–700 kJ/mol. for α-$Al_2O_3$ [8, 66–69]. But, superimposing the $k_p$ data of the present work in Arrhenius plots from the literature indicates good agreement [53].

RE-doped $Fe_3Al$–Zr, during isothermal oxidation, produced better adherence of the oxide scale and even slowed down the oxide growth rate in comparison with undoped $Fe_3Al$. The effect of Zr is clearly shown at higher temperatures. As an example, the total weight gain after 100 h oxidation $Fe_3Al$ at 1200 °C achieved ∼3.7 mg/cm². It was about three times more than for doped $Fe_3Al$–Zr. Similar results were observed for cast Fe–Al alloy, ODS Fe–Al alloys and Fe–40Al–0.07Zr [68, 69].

Cyclic-oxidation experiments showed that for undoped $Fe_3Al$, breakaway oxidation occurred after a few (about 5) cycles, the sample being then totally transformed in non-protective iron oxide, $Fe_2O_3$. $Fe_3Al$–Zr alloy showed iron–oxide crystals on the surface near edges and corners after 80 cycles, respectively. Zr additions did not prevent breakaway, but delayed it, thus improving the lifetime of the samples. However, REE appears much less important compared to FeCrAl alloys [32–34]. Wright et al. [36] proposed the reason is that thermal-expansion coefficient of $Fe_3Al$ is higher than that of FeCrAl, leading to higher thermal stress and then spallation. It was evidenced by TEC measurements performed in Oak Ridge National Laboratory [39]. Pint et al. also proposed that iron aluminides with Zr can internally nitride in air, causing shorter life [70, 71].

Oxygen-marker experiments showed that, with and without Zr, θ-$Al_2O_3$ grew mainly at 900 °C via diffusion of aluminium cations, as previously proposed by Pint et al. [72]. At 1100 °C, the RE-free alloys oxidized by simultaneous outward-aluminum and inward-oxygen diffusion through the oxide scale, forming equiaxed, coarse-oxide grains; whereas, RE-doped alumina-forming alloys oxidize by inward-oxygen diffusion along thin, columnar-oxide grain boundaries; this is in accordance to previous studies [22, 44, 46, 73]. TEM specimen cross-sections observed on $Fe_3Al$–Zr after 100 h at 1100 °C revealed second-phase particles were rich in Zr (identified as $ZrO_2$) at the metal–oxide interface. Zr was also found to segregate at alumina grain boundaries, which is consistent with many papers dealing with RE segregation at alumina grain boundaries (see compilation in references [49, 74]). Zr segregation could be directly related to a change in the growth mechanism from predominant cation to predominant anion diffusion along $Al_2O_3$ grain boundaries. As a consequence, it provokes a change in the microstructure of the $Al_2O_3$ scale which consists of columnar oxide grains, in addition to the equiaxed grains formed at the initial stage of oxidation, as already observed in FeCrAl alloys doped with RE [51].

## Conclusions

The present work provided a detailed comparison of oxidation behaviors of $Fe_3Al$ with and without Zr in air in the temperature range of 900–1200 °C. The results based on specimen mass changes and microstructural characterizations indicated

that Zr additions significantly improved the oxidation resistance of these alloys. Thus, the oxidation products were duplex scales with well-developed columnar grains covered by fine equiaxial grains.

Zr additions improved the adherence of the $\alpha$-Al$_2$O$_3$ scale, but only limited breakaway kinetics (80 24 h-cycles at 1100 °C against 3 for undoped Fe$_3$Al). Zr segregation was observed at alumina grain boundaries at 1100 °C. Two-stage oxidation experiments confirmed that $\theta$-Al$_2$O$_3$ mainly grew by cation diffusion in Fe$_3$Al and Fe$_3$Al–Zr at 900 °C. At 1100 °C, $\alpha$-Al$_2$O$_3$ formed via a mixed diffusion process on Fe$_3$Al, whereas formed by anion diffusion in Fe$_3$Al–Zr, in relation with Zr segregation at alumina grain boundaries.

# References

 1. J. H. Westbrook, *Intermetallic Compounds* (John Wiley & Sons Inc, New York, 1960).
 2. P. F. Tortorelli and K. Natesan, *Materials Science Engineering A* **258**, 115 (1998).
 3. K. Natesan, *Materials Science Engineering A* **258**, 126 (1998).
 4. C. G. McKamey, J. H. DeVan, P. F. Tortorelli, and V. K. Sikka, *Journal of Materials Research* **6**, 1779 (1991).
 5. W. E. Boggs, *Journal of the Electrochemical Society* **118**, 906 (1971).
 6. J. L. Smialek, J. Doychak, and D. J. Gaydosh, *Oxidation of Metals* **34**, 259 (1990).
 7. I. Rommerskirchen, B. Eltester, and H. J. Grabke, *Materials Corrosion* **47**, 646 (1996).
 8. C. H. Xu, W. Gao, and H. Gong, *Intermetallics* **8**, 769 (2000).
 9. C. H. Xu, W. Gao, and D. Li, *Corrosion Science* **43**, 671 (2001).
10. P. Tomaszewicz, in *High Temperature Corrosion*, ed. R. A. Rapp (NACE, Houston, USA, 1983), p. 258.
11. W. J. Quadakkers and M. J. Bennett, *Materials Science Technology* **10**, 126 (1994).
12. B. A. Pint, L. R. Walker, and I. G. Wright, *Materials at High Temperature* **21**, 175 (2004).
13. W. J. Quadakkers and M. J. Bennet, *Materials Sciences and Technology* **10**, 126 (1994).
14. R. Klumpes, The influence of chromium on the oxidation of b-NiAl at 1000°C. in *Oxidation of Intermetallics*, ed. H. J. Grabke (Wiley VCH, 1998), p. 99.
15. G. C. Wood, *Oxidation of Metals* **2**, 11 (1970).
16. P. F. Tortorelli and J. H. DeVan, *Materials Sciences Engineering A* **154**, 1065 (1992).
17. J. H. DeVan and P. F. Tortorelli, *Materials at High Temperature* **11**, 30 (1993).
18. S. C. Deevi and V. K. Sikka, *Intermetallics* **4**, 357 (1996).
19. Z. Liu and W. Gao, *Oxidation of Metals* **54**, 189 (2000).
20. Z. G. Zhang, F. Gesmundo, P. Y. Hou, and Y. Niu, *Corrosion Science* **48**, 741 (2006).
21. D. P. Whittle and J. Stringer, *Philosophical Transactions of the Royal Society of London* **295**, 309 (1980).
22. F. H. Stott, G. C. Wood, and J. Stringer, *Oxidation of Metals* **44**, 113 (1995).
23. B. A. Pint, *Oxidation of Metals* **45**, 1 (1996).
24. W. J. Quadakkers and L. Singheiser, *Materials Science Forum* **369–372**, 77 (2001).
25. J. Jedlinski, *Solid State Ionics* **101–103**, 1033 (1997).
26. R. Cueff, H. Buscail, E. Caudron, C. Issartel, and R. Riffard, *Oxidation of Metals* **58**, 439 (2002).
27. J. K. Tien and F. S. Pettit, *Metallurgical Transaction* **3**, 1587 (1972).
28. R. Prescott and M. J. Graham, *Oxidation of Metals* **38**, 233 (1992).
29. J. Jedlinski, *Oxidation of Metals* **39**, 55 (1993).
30. K. Y. Kim, *Oxidation of Metals* **41**, 179 (1994).
31. S. Taniguchi, *Materials and Corrosion* **48**, 1 (1997).

32. S. Chevalier, G. Strehl, H. Buscail, G. Borchardt, and J. P. Larpin, *Materials and Corrosion* **55**, 352 (2004).
33. S. Chevalier, A. P. D. Tankeu, H. Buscail, C. Issartel, G. Borchardt, and J. P. Larpin, *Materials and Corrosion* **55**, 610 (2004).
34. S. Chevalier, G. Strehl, H. Buscail, C. Issartel, G. Borchardt, and J. P. Larpin, *Materials and Corrosion* **57**, 476 (2006).
35. C. Houngninou, S. Chevalier, and J. P. Larpin, *Oxidation of Metals* **65**, 409 (2006).
36. I. G. Wright, B. A. Pint, and P. F. Tortorelli, *Oxidation of Metals* **55**, 333 (2001).
37. B. A. Pint, P. F. Tortorelli, and I. G. Wright, *Materials and Corrosion* **47**, 663 (1996).
38. B. A. Pint, P. F. Tortorelli, and I. G. Wright, *Materials at High Temperature* **16**, 1 (1999).
39. B. A. Pint, K. L. More, P. F. Tortorelli, W. D. Porter, and I. G. Wright, *Materials Science Forum* **369–372**, 411 (2001).
40. K. Przybylski, A. J. Garratt-Reed, B. A. Pint, E. P. Katz, and G. J. Yurek, *Journal of the Electrochemical Society* **134**, 3207 (1987).
41. K. P. R. Reddy, J. L. Smialek, and A. R. Cooper, *Oxidation of Metals* **17**, 429 (1982).
42. B. A. Pint, J. R. Martin, and L. W. Hobbs, *Oxidation of Metals* **39**, 167 (1993).
43. S. Chevalier, C. Nivot, and J. P. Larpin, *Oxidation of Metals* **61**, 195 (2004).
44. W. J. Quadakkers, H. Holzbrecher, K. G. Briefs, and H. Beske, *Oxidation of Metals* **32**, 67 (1989).
45. W. J. Quadakkers, W. Speier, H. Holzbrecher, and H. Nickel, SIMS investigations of the transport phenomena in chromia and alumina scales on ODS alloys. in *Proc. Conference on Microscopy of Oxidation, Cambridge, UK, March 1990* (1991), p. 149.
46. C. Mennicke, E. Schumman, M. Ruhle, K. J. Hussey, G. I. Sproule, and M. J. Graham, *Oxidation of Metals* **49**, 455 (1998).
47. P. Nanni, C. T. H. Stoddart, and E. D. Hondros, *Journal of Materials Chemistry* **1**, 297 (1973).
48. S. Chevalier, B. Lesage, C. Legros, G. Borchardt, G. Strehl, and M. Kilo, *Defect and Diffusion Forum* **237–240**, 899 (2005).
49. S. Chevalier, *Traitement de surface et nouveaux matériaux: quelles solutions pour lutter contre la dégradation des matériaux métalliques à haute température?*, (Les Editions Universitaires de Dijon, Dijon, 2007), p. 61.
50. S. Chevalier, G. Bonnet, G. Borchardt, J. C. Colson, and J. P. Larpin, *Materials Science Forum* **369–372**, 327 (2001).
51. S. Chevalier, K. Przybylski, G. Borchardt, and J. P. Larpin, *Materials Science Forum* **461–464**, 53 (2004).
52. N. Babu, R. Balasubramaniam, and A. Ghosh, *Corrosion Science* **43**, 2239 (2001).
53. D. B. Lee, G. Y. Kim, and J. G. Kim, *Materials Science and Engineering A* **339**, 109 (2003).
54. Z. G. Yang and P. Y. Hou, *Materials Science and Engineering A* **391**, 1 (2005).
55. S. Chevalier, A. Galerie, O. Heintz, R. Chassagnon, and A. Crisci, *Materials Science Forum* **595–598**, 915 (2008).
56. J. Fedotova, G. Bonnet, F. Pedraza, J. Balmain, S. Dubois, V. Gauthier, M. F. Denanot, N. OuabadiI, A. Letsko, A. Ilvuschenko, and A. Akimov, *Corrosion Science* **50**, 1693 (2008).
57. D. Monceau and B. Pieraggi, *Oxidation of Metals* **50**, 477 (1998).
58. G. C. Wood, *Werkstoffe und Korrosion* **22**, 491 (1971).
59. F. A. Golightly, G. C. Wood, and F. H. Stott, *Oxidation of Metals* **14**, 217 (1980).
60. T. A. Ramanarayanan, R. Ayer, R. Petkovic-Luton, and D. P. Leta, *Oxidation of Metals* **29**, 445 (1988).
61. W. C. Hagel, *Corrosion* **21**, 316 (1965).
62. G. C. Rybicki and J. L. Smialek, *Oxidation of Metals* **31**, 275 (1989).
63. M. W. Brumm and H. J. Grabke, *Corrosion Science* **33**, 1677 (1992).
64. H. J. Grabke, *Materials Science Forum* **251–254**, 149 (1997).
65. E. Andrieu, A. Germidis, and R. Molins, *Materials Science Forum* **251–254**, 357 (1997).
66. T. V. Mani, P. K. Pallai, A. D. Damodaran, and K. G. K. Warrier, *Materials Letters* **19**, 237 (1994).
67. S. J. Wilson and J. C. D. McConnell, *Journal of Solid State Chemistry* **34**, 315 (1980).
68. C. Chan, C. Huvier, and J. F. Dinhut, *Intermetallics* **9**, 817 (2001).
69. F. Lang, Z. Yu, S. Gedevanishvili, S. C. Deevi, and T. Narita, *Intermetallics* **11**, 697 (2003).
70. C.-H. Xu, W. Gao, and Y.-D. He, *Scripta Materialia* **42**, 975 (2000).
71. B. A. Pint, J. R. Regina, K. Prïssner, L. D. Chitwood, K. B. Alexander, and P. F. Tortorelli, *Intermetallics* **9**, 735 (2001).
72. B. A. Pint, J. R. Martin, and L. W. Hobbs, *Solid State Ionics* **78**, 99 (1995).

73. B. A. Pint, A. J. Garratt-Reed, and L. W. Hobbs, *Materials at High Temperature* **13**, 3 (1995).
74. S. Chevalier, in *Developments in High-Temperature Corrosion and Protection of Materials*, eds. G. Wei and L. Zhengwei, Chap. 10 (Woodhead Publishing in Materials, Cambridge, England, 2008), p. 290.